RESWARA: Jurnal Riset Ilmu Teknik
2026, Vol. 4, No. 3, pp. 811-830
E-ISSN: 3025-9444

Mechanism-Driven Performance Limitations in $FASnI_3$ Perovskite Solar Cells: A SCAPS-1D Study of the ITO/ZnO/$FASnI_3$/NiO/Pt Architecture

Abi Nurhidayat [1]✉, Bambang Soegijono [2]
(1,2) Study Program of Physics, Institut Sains dan Teknologi Nasional, Jakarta, Indonesia

Abstract: *Lead-free $FASnI_3$ perovskite solar cells offer a promising route toward environmentally benign photovoltaics, yet their practical performance remains constrained by unresolved loss mechanisms and overly idealized simulation assumptions. This study presents a mechanism-resolved SCAPS-1D analysis of the ITO/ZnO/$FASnI_3$/NiO/Pt architecture by evaluating the contributions of bulk recombination, interface recombination, resistive losses, and temperature effects within a unified framework. A graded realistic-defect methodology is introduced to bridge the gap between near-ideal simulations and fabrication-relevant conditions. Comprehensive parameter sweeps were performed for absorber energetics, doping concentration, thickness, bulk and interface defect densities, transport-layer properties, series resistance, operating temperature, and back-contact work function, while incorporating Shockley–Read–Hall, radiative, and Auger recombination mechanisms. Under near-ideal low-defect conditions, the optimized device achieves $V_{oc} = 1.123V$, $J_{sc} = 31.88mA\ cm^{-2}$, FF = 89.04%, and PCE = 31.90%, representing an upper-bound estimate within the simplified optical model. Under realistic conditions, the efficiency decreases systematically to 28.80% for the typical scenario, 22.57% for the moderate scenario, and 15.06% for the pessimistic scenario. The results establish a clear hierarchy of performance-limiting mechanisms, with bulk and interface Shockley–Read–Hall recombination dominating the efficiency gap, followed by series resistance and thermal effects. These findings provide a transferable mechanism-based framework and practical design guidelines for improving high-efficiency, lead-free $FASnI_3$ perovskite solar cells beyond idealized simulation conditions.*

Article history:
Received: 11 July 2026
Revised: 26 July 2026
Accepted: 28 July 2026
Published: 29 July 2026

Keyword:
$FASnI_3$, SCAPS-1D, Sn-based perovskite, Solar Cells

This is an open-access article under the CC-BY-SA License.

How to cite: Nurhidayat, A., & Soegijono, B. (2026). Mechanism-Driven Performance Limitations in $FASnI_3$ Perovskite Solar Cells: A SCAPS-1D Study of the ITO/ZnO/$FASnI_3$/NiO/Pt Architecture. *RESWARA: Jurnal Riset Ilmu Teknik*, *4*(3), 811–830. https://doi.org/10.70716/reswara.v4i3.736

INTRODUCTION

Solar energy is widely recognized as one of the most promising renewable energy sources for reducing carbon emissions and dependence on fossil fuels (Ateeq ul Rehman et al., 2024). In this context, perovskite solar cells (PSCs) have attracted extensive attention owing to their rapid efficiency improvement, simple fabrication routes, and potential for low-cost photovoltaic production. The ABX_3 perovskite structure offers favorable optoelectronic properties, including strong optical absorption, tunable bandgap, high carrier mobility, and long diffusion length, making PSCs highly attractive for next-generation solar-energy conversion technologies (Hussein Sabbah, 2022).

Despite these advantages, the practical deployment of PSCs remains hindered by the toxicity concerns associated with lead-based perovskites. This issue has stimulated the development of lead-free alternatives, among which tin (Sn)-based perovskites are considered one of the most promising candidates. In particular, formamidinium tin iodide ($FASnI_3$) has emerged as an attractive absorber

✉ *Corresponding author:* ***abinurhidyat@gmail.com***
Copyright © 2026, the author(s)

material because its bandgap is close to the optimum range for single-junction photovoltaics and is also compatible with tandem-device applications. However, the practical performance of $FASnI_3$-based PSCs remains limited by several coupled challenges, including the oxidation of Sn^{2+} to Sn^{4+}, high bulk defect density, strong non-radiative recombination, interface trap states, energetic mismatch at charge-selective contacts, and resistive losses that reduce the open-circuit voltage (V_{oc}), fill factor (FF), and overall power conversion efficiency (PCE) (Hussein Sabbah, 2022; Ateeq ul Rehman et al., 2024; Mustafa et al., 2026).

Recent simulation-driven reports have explored performance enhancement in lead-free PSCs by varying transport layers, absorber compositions, and device architectures. Ahmad et al. optimized an $FASnI_3$-based device using SCAPS and reported improved performance with Jsc = 31.20 mA/cm², Voc = 1.81 V, FF = 33.72%, and PCE = 19.08% (Ahmad et al., 2023). Nalianya et al. obtained a PCE of 18.79% for an FTO/PCBM/$CsSn_{0.5}Ge_{0.5}I_3$/Spiro-OMeTAD/Au stack (Nalianya et al., 2021), while Sajid et al. showed that HTL-free $CsSnI_3$ devices can reach 19.03% when the bulk defect density is maintained around 10^{15} cm^{-3} (Sajid et al., 2023). For inverted p–i–n $FASnI_3$ configurations, efficiencies around 17–18% have been linked to long carrier lifetimes (τ > 50 ns) and reduced SRH recombination losses (Shukla et al., 2021). Additional studies reported PCE values of 17.74% for $CH_3NH_3GeI_3$ using Spiro-OMeTAD (Jan & Noman, 2022) and 16.05% for $FASnI_3$ devices employing $CuSbS_2$ as an HTL (Azhakanantham et al., 2022). Chabri et al. achieved 15.68% in $CsGeI_3$ through bulk/interface defect optimization (Chabri et al., 2023), whereas the FTO/ZnO/$FASnI_3$/Cu_2O/Au structure yielded only 7.83% in another report (Masood Mehrabian 1 & 3, 2024). More recently, Ateeq ul Rehman et al. reported a higher simulated efficiency of 24.87% using an FTO/CeO_2/$FASnI_3$/CuI/Au architecture (Ateeq ul Rehman et al., 2024).

These studies have provided useful insight into parameter sensitivity and architectural design. Previous SCAPS-1D studies have provided important insights into the optimization of Sn-based and lead-free perovskite solar cells by varying absorber properties, transport layers, defect densities, and device architectures. However, most reported studies primarily focus on obtaining a single optimized efficiency through individual parameter variations. The effects of bulk recombination, interface recombination, series resistance, temperature, and intrinsic recombination are rarely evaluated within a common and internally consistent device framework. Consequently, the relative importance of these loss mechanisms and the transition from idealized simulation performance to fabrication-relevant operating conditions remain insufficiently resolved.

The novelty of the present study lies in the integration of parameter optimization and mechanism-resolved performance assessment within a unified SCAPS-1D framework. First, controlled single-parameter sweeps are used to evaluate the effects of absorber bandgap, electron affinity, acceptor concentration, thickness, bulk defect density, interface defect density, series resistance, temperature, and contact properties. Second, a graded realistic-defect framework is introduced by defining near-ideal, typical, moderate, and pessimistic scenarios under a consistent treatment of Shockley–Read–Hall, radiative, and Auger recombination. This approach enables the study not only to estimate an optimized upper-bound performance, but also to quantify the progressive efficiency loss under increasingly realistic material and operational conditions.

Accordingly, this study aims to: (i) determine a physically consistent parameter window for the ITO/ZnO/$FASnI_3$/NiO/Pt architecture; (ii) quantify the transition from near-ideal to fabrication-relevant device performance; and (iii) establish a hierarchy of the dominant performance-limiting

Copyright © 2026, the author(s). This is an open access article under the CC-BY-SA License.

mechanisms. Rather than presenting the highest simulated efficiency as a directly achievable experimental value, the proposed framework distinguishes theoretical potential from practically relevant performance and translates the resulting loss hierarchy into material- and interface-engineering priorities for $FASnI_3$ solar cells.

RESEARCH METHOD

Benchmark Review of Related Simulation Studies

Tabel 1. Benchmark Review of Related Simulation Studies

Reference	Device architecture	Simulator	Voc (V)	Jsc (mA/cm^2)	FF (%)	PCE (%)
(Singh, 2024)	FTO/TiO_2/$FASnI_3$/Spiro-OMeTAD	SCAPS	1.81	31.20	33.72	19.08
(Shukla, 2021)	ITO/C60/$FASnI_3$/PEDOT:PSS	SCAPS	0.806	25.2	83.62	17.33
(Azhakanantham, 2022)	FTO/C60/$FASnI_3$/Spiro-OMeTAD	SCAPS	0.65	26.93	58.79	10.25
(Mehrabian, 2024)	FTO/ZnO/$FASnI_3$/Cu_2O/Au	SCAPS	0.76	12.26	64.91	7.83
(El Arfaoui et al., 2024)	FTO/ZnO/$FASnI_3$/Spiro-OMeTAD	SCAPS	1.06	16.71	85.85	19.80
(Lakhili & Qjidaa, 2024)	FTO/$ZnO_{0.25}S_{0.75}$/$FASnI_3$/Mg–$CuCrO_2$	SCAPS	0.7725	25.5612	76.50	15.11
(Noman et al., 2024)	FTO/PCBM/$FAPbI_3$/CuI	SCAPS	1.14	21.64	70.93	17.61
(Ateeq ul Rehman et al., 2024)	FTO/CeO_2/$FASnI_3$/CuI/Au	SCAPS	0.9308	30.675	87.10	24.87

To position the present study within the existing field, representative SCAPS-based reports on lead-free and Sn-based perovskite solar cells were first reviewed as contextual benchmarks. Because the reported photovoltaic metrics in the literature depend strongly on differences in device architecture, optical assumptions, recombination models, bulk and interface defect densities, and contact parameters, these studies were not used as direct one-to-one performance references. Instead, the benchmark comparison was used to place the selected $FASnI_3$-based architecture in context and to motivate a mechanism-oriented analysis rather than a simple efficiency competition.

Device Structure and Simulation Conditions

The photovoltaic performance of the proposed device was investigated using the one-dimensional Solar Cell Capacitance Simulator, SCAPS-1D (version 3.3.12). The simulated planar superstrate device consisted of the stack ITO/ZnO/$FASnI_3$/NiO/metal, where ITO served as the transparent conducting oxide, ZnO as the electron transport layer (ETL), $FASnI_3$ as the absorber layer,

Copyright © 2026, the author(s). This is an open access article under the CC-BY-SA License.

and NiO as the hole transport layer (HTL). Unless otherwise stated, Pt was used as the baseline back-contact metal because of its high work function and favorable hole-extraction characteristics.

Illumination was applied from the ITO side under the standard superstrate configuration. Unless otherwise specified, all simulations were carried out under AM1.5G illumination with an incident power density of 100 mW cm^{-2} at a baseline operating temperature of 300 K. This reference structure was used as the starting point for all subsequent parametric sweeps and limiting-condition analyses.

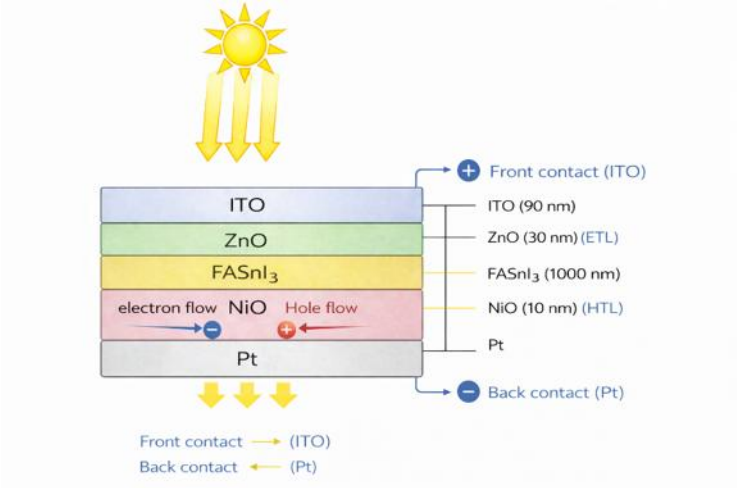

Figure 1 Device Structure

Governing Physical Model

The device simulations were performed using the one-dimensional solar-cell capacitance simulator SCAPS-1D (v3.3.12), which solves the coupled semiconductor transport equations under steady-state conditions. The electrostatic potential distribution across the multilayer stack is obtained from Poisson's equation (Ateeq ul Rehman et al., 2024):

$$\frac{\partial^2 \varphi}{\partial x^2} + \frac{q}{\varepsilon}\left[p(x) - n(x) + N_D - N_A + \rho_p - \rho_n\right] = 0 \quad (1)$$

where φ is the electrostatic potential, q is the elementary charge, ε is the dielectric permittivity, $n(x)$and $p(x)$ are the electron and hole concentrations, $N_D$and $N_A$denote the ionized donor and acceptor densities, and $\rho_p$and $\rho_n$represent charge contributions associated with defect states. Carrier transport is described by the continuity equations for holes and electrons(Ateeq ul Rehman et al., 2024):

$$\frac{1}{q}\frac{dJ_p}{dx} = G_{\mathrm{op}}(x) - R(x) \quad (2)$$

$$\frac{1}{q}\frac{dJ_n}{dx} = -G_{\mathrm{op}}(x) - R(x) \quad (3)$$

where $J_p$and $J_n$are the hole and electron current densities, $G_{\mathrm{op}}(x)$is the position-dependent optical generation rate, and $R(x)$is the net recombination rate. The current densities are computed

Copyright © 2026, the author(s). This is an open access article under the CC-BY-SA License.

using the drift–diffusion formalism, in which carrier transport arises from the combined effects of the electric field (drift) and concentration gradients (diffusion). Boundary conditions are applied at the front and back contacts through the specified metal work function and surface recombination velocities, enabling the extraction of J–V characteristics and photovoltaic metrics (Voc, Jsc, FF, and PCE) under the chosen illumination, temperature, and resistive settings.

To maintain physically meaningful performance limits, three recombination pathways were included throughout the simulations: defect-assisted Shockley-Read-Hall (SRH) recombination, radiative recombination, and Auger recombination. SRH recombination was used to represent carrier loss through bulk and interface traps, while the radiative and Auger terms were incorporated to avoid overestimating the intrinsic device ceiling. The radiative recombination coefficient was fixed at $3 \times 10^{-11}\mathrm{cm}^3\ \mathrm{s}^{-1}$, and the Auger coefficients were taken as $C_n = C_p = 1 \times 10^{-28}\mathrm{cm}^6\ \mathrm{s}^{-1}$, unless otherwise stated. Resistive losses were introduced through an explicit series resistance (R_s), and temperature-dependent behavior was examined by varying the operating temperature in the defined simulation scenarios (Al-mousoi et al., 2023;Park et al., 2024).

Optical generation was modeled using the built-in SCAPS absorption formulation (bandgap-based model). Therefore, the absolute value of Jsc may differ if a measured/digitized absorption coefficient α(λ) is employed; however, the comparative trends and electrical-loss insights derived from controlled parameter sweeps remain valid within this modeling framework. Unless stated otherwise, simulations were performed under AM1.5G, 100 mW cm^{-2} (1 sun)(Ateeq ul Rehman et al., 2024).From the simulated J–V curves, the key photovoltaic metrics were extracted: open-circuit voltage (Voc), short-circuit current density (Jsc), fill factor (FF), and power conversion efficiency (PCE). Each parametric sweep was performed by varying a single parameter while keeping the remaining parameters fixed at their baseline values, enabling attribution of performance changes to specific physical mechanisms.

Baseline Parameters and Optimization Workflow

Material parameters for each layer were adopted from representative device models and literature-consistent settings, and then refined through a staged optimization workflow:

Tabel 2. The fundamental parameters used in the simulation of $FASnI_3$-based perovskite solar cell

Electrical Parameter	NiO	$FASnI_3$	ZnO	ITO
Bandgap (eV)	3.7	1.47	3.3	3.5
Relative permittivity, εr	10.70	8.2	9.0	9.0
Thickness (nm)	10	450	30	90
CB effective density of states	2×10^{19}	1×10^{18}	2×10^{18}	2.2×10^{18}
VB effective density of states	1×10^{19}	1×10^{18}	1.8×10^{19}	1.8×10^{19}
Electron affinity (ev)	2.1	4.0	4.0	4.0

Copyright © 2026, the author(s). This is an open access article under the CC-BY-SA License.

Electron mobility (cm^2/Vs)	12.0	22.0	100	20.0
Hole mobility (cm^2/Vs)	2.0	22.0	25.0	10.0
Uniform donor density ND (cm^3)	0.0	0.0	1×10^{18}	1×10^{21}
Uniform acceptor density NA (cm^3)	1.6×10^{14}	7.0×10^{16}	0.0	0.0
Electron thermal velocity (cm/s)	1.0×10^{7}	1.0×10^{7}	1.0×10^{7}	1.0×10^{7}
Hole thermal velocity(cm/s)	1.0×10^{7}	1.0×10^{7}	1.0×10^{7}	1.0×10^{7}
Defect density Nt	1.0×10^{15}	1.0×10^{15}	1.0×10^{15}	1.0×10^{15}
Reference	(Mouchou et al., 2021)	(Ateeq ul Rehman et al., 2024; Hussein Sabbah, 2022)	(Aseena et al., 2020)	(Njema et al., 2025)

Table 2 summarizes the electrical and optical input parameters used to build the baseline NiO/$FASnI_3$/ZnOITO device in SCAPS-1D. These values were adopted from representative literature reports for each layer to ensure physical plausibility and reproducibility, covering fundamental material descriptors such as bandgap, electron affinity, relative permittivity, effective density of states, carrier mobilities, and doping densities. The thicknesses were set to typical experimentally relevant ranges (NiO: 10 nm, $FASnI_3$: 450 nm, ZnO: 30 nm, ITO: 90 nm), providing a realistic starting point prior to parametric optimization. Unless explicitly varied in the subsequent sweeps, the parameters in Table 2 were kept fixed to isolate the effect of the investigated variable. Importantly, the initial bulk defect density (N_t) was set to $1 \times 10^{15}\,\mathrm{cm}^{-3}$ for all layers as a literature-based baseline, which was later adjusted to construct near-ideal and realistic defect scenarios and to quantify performance sensitivity to defect-related SRH recombination.

Tabel 3. The fundamental parameters used in the simulation Interface parameters of layers

Parameters	P-NiO/$FASnI_3$	$FASnI_3$/N-ZnO
Defect Type	Neutral	Neutral
Capture cross section for electrons (cm^2)	1×10^{-15}	1×10^{-15}
Capture cross section for hole (cm^2)	1×10^{-15}	1×10^{-15}
Energetic distribution Single	Single	Single
Energy concerning Reference (eV)	0.6	0.6

Copyright © 2026, the author(s). This is an open access article under the CC-BY-SA License.

Characteristic energy/Ev	0.1	0.1
Total density (integrated over all energies) ($1/cm^2$)	1.0×10^{12}	1.0×10^{12}
Reference	(Ateeq ul Rehman et al., 2024)	(Ateeq ul Rehman et al., 2024)

Interface recombination was modeled using a neutral defect-state distribution at the two dominant heterointerfaces, NiO/$FASnI_3$ and $FASnI_3$/ZnO, as listed in Table 2. a single-level energetic distribution was assumed with the defect energy positioned at 0.6 eV relative to the valence-band reference, and electron/hole capture cross-sections were set to $1 \times 10^{-15}\,cm^2$ (Ateeq ul Rehman et al., 2024), consistent with commonly used SCAPS parameterization for perovskite interfaces. The baseline integrated interface defect density was fixed at $1 \times 10^{12}\,cm^{-2}$for both interfaces to represent a relatively well-passivated condition(Ateeq ul Rehman et al., 2024). In later sections, the interface defect density was increased simultaneously at both interfaces to emulate progressively degraded interfacial quality and to evaluate the transition from near-ideal to realistic device operation

Final Optimized Parameter Set Used in the Simulations

Table 4. Final optimized parameter absorber $FASnI_3$ set used for the baseline device simulations

Parameter	Value	Notes
Absorber bandgap	1.39 eV	optimum from bandgap sweep
Electron affinity (χ)	4.05 eV	best band alignment
Acceptor doping (NA)	$7 \times 10^{17} cm^{-3}$	optimized under Auger-included model
Absorber thickness	1000 nm	compromise between absorption and recombination
Bulk defect density	$1 \times 10^{12} cm^{-3}$	varied in realistic scenarios (near-ideal)
Interface defect density	$1 \times 10^{12}\ cm^{-2}$	baseline condition
Series resistance	~0 Ω·cm²	ideal case
Temperature	300 K	baseline
Back contact	Pt	high work function contact
Radiative coefficient (B)	$3\times10^{-11}\ cm^3\ s^{-1}$	literature value
Auger coefficient (Cn = Cp)	$1\times10^{-28}\ cm^6\ s^{-1}$	literature value

After the sequential parameter sweeps described above (bandgap, electron affinity, absorber doping, thickness, bulk defects, and interface traps), a consistent optimized parameter set was selected to serve as the baseline configuration for the near-ideal and realistic device scenarios. Table 4 summarizes the final optimized parameters adopted in the subsequent simulations and performance-limitation analysis.

Copyright © 2026, the author(s). This is an open access article under the CC-BY-SA License.

Limiting-Condition Scenarios for Device Performance Evaluation

Tabel 5. Limiting-condition scenarios used to evaluate device performance degradation

Setting (dominant non-idealities)	Near-ideal	Typical	Moderate	Pessimistic
$FASnI_3$ bulk N_t (cm^{-3})	1.0×10^{12}	1.0×10^{15}	1.0×10^{16}	1.0×10^{17}
NiO bulk N_t (cm^{-3})	1.0×10^{12}	1.0×10^{15}	1.0×10^{15}	1.0×10^{16}
ZnO bulk N_t (cm^{-3})	1.0×10^{12}	1.0×10^{15}	1.0×10^{15}	1.0×10^{16}
ITO bulk N_t (cm^{-3})	1.0×10^{12}	1.0×10^{15}	1.0×10^{15}	1.0×10^{15}
Interface N_t (NiO/$FASnI_3$) (cm^{-2})	$\leq1.0\times10^{12}$	1.0×10^{13}	1.0×10^{14}	1.0×10^{15}
Interface N_t ($FASnI_3$/ZnO) (cm^{-2})	$\leq1.0\times10^{12}$	1.0×10^{13}	1.0×10^{14}	1.0×10^{15}
Series resistance Rs ($\Omega\cdot cm^2$)	~0	0.5	1	2
Temperature (K)	300	300	320	340
Radiative B (cm^3/s)	3.0×10^{-11}	3×10^{-11}	3.0×10^{-11}	3.0×10^{-11}
Auger Cn=Cp (cm^6/s)	1.0×10^{-28}	1.0×10^{-28}	1.0×10^{-28}	1.0×10^{-28}

Because Sn-based perovskite parameters vary across studies, the selected values are treated as a consistent baseline rather than fixed constants. The analysis therefore focuses on comparative trends and dominant loss mechanisms. The device was evaluated under near-ideal and graded realistic scenarios by increasing bulk and interface defects, series resistance, and temperature. Table 5 summarizes the resulting performance range and the main non-idealities responsible for efficiency degradation.

RESULTS AND DISCUSSION

Effects of Absorber Bandgap and Electron Affinity

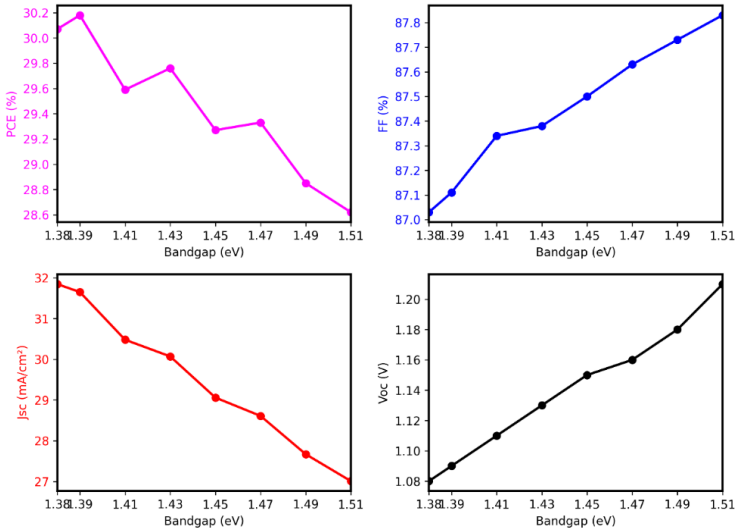

Figure 2. Influence of absorber (perovskite) bandgap on solar-cell performance parameters: Voc, Jsc, FF, and PCE

Copyright © 2026, the author(s). This is an open access article under the CC-BY-SA License.

The key advantage of halide perovskites is the tunability of their bandgap, which enables deliberate control over optical absorption, carrier generation, and the voltage–current trade-off in perovskite solar cells (PSCs) (Ibarra Michel et al., 2022) . In general, reducing the absorber bandgap extends the absorption edge toward longer wavelengths, thereby increasing photogeneration and potentially enhancing J_{sc}, while a larger bandgap can raise the maximum achievable $V_{oc}$by increasing the quasi-Fermi level splitting. However, an excessively small bandgap may increase carrier recombination and weaken charge separation, whereas an overly large bandgap reduces the fraction of incident photons with energies above E_g, limiting photocurrent. Therefore, an optimal bandgap must balance absorption-driven current gain against voltage and recombination losses to maximize device efficiency (Hussein Sabbah, 2022).

In this study, the $FASnI_3$ absorber bandgap was varied from 1.38 to 1.51 eV (Fig. 2). The results show that increasing $E_g$produces a monotonic rise in $V_{oc}$from 1.08 V (1.38 eV) to 1.206 V (1.51 eV), while J_{sc}decreases from 31.845 to 27.01 mA/cm^{-2} because the absorption window narrows. Meanwhile, the fill factor changes only slightly (from 87.03% to 87.83%), indicating that the device remains close to a stable extraction regime across this range and that the performance variation is mainly governed by the fundamental V_{oc}–J_{sc} compromise. As a consequence, the PCE does not increase monotonically with bandgap; instead, it exhibits a clear optimum at an intermediate value.Specifically, the maximum efficiency is obtained at $E_g = 1.39\ eV$, $delivering\ Voc = 1.09\ V$, Jsc= 31.65 mA/cm^2,FF = 87.11%, and PCE = 30.18%. At slightly lower bandgap (1.38 eV), the higher current is insufficient to compensate for the reduced V_{oc}, while at higher bandgaps (≥1.45 eV) the incremental voltage gain is outweighed by the stronger photocurrent reduction, resulting in lower PCE. Overall, these trends underline the coupled roles of optical absorption and voltage-limiting mechanisms in determining device performance under bandgap variation, and they identify ~1.39 eV as the most suitable bandgap for further optimization of band alignment and defect-related losses in the proposed NiO/$FASnI_3$/ZnOITO architecture.

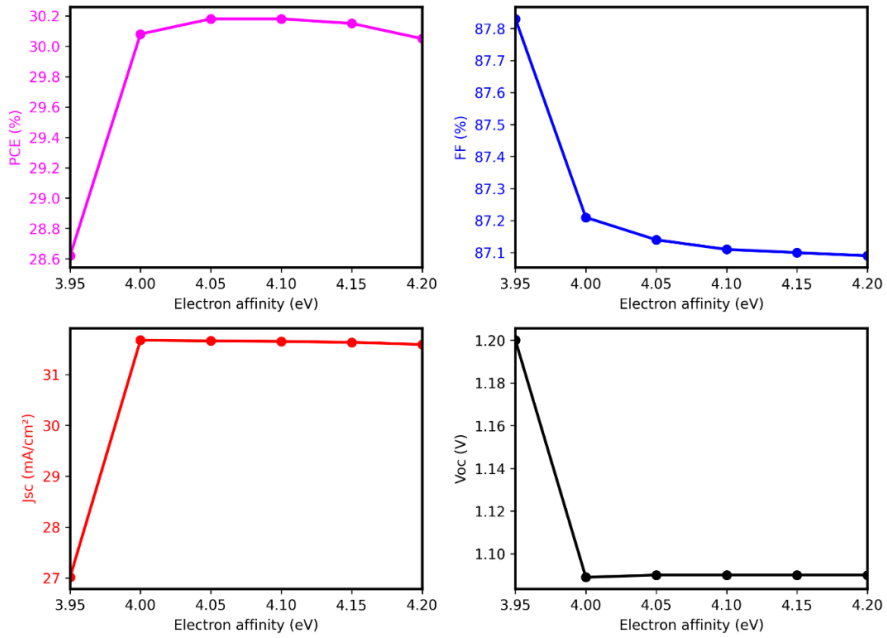

Figure 3. Effect of $FASnI_3$ electron affinity on photovoltaic performance parameters (Voc, Jsc, FF, and PCE)

The electron affinity is the amount of energy required for obtaining a released electron from the perovskite layer's maximum occupied mo lecular orbiting (HOMO) to the lowest unoccupied molecular

Copyright © 2026, the author(s). This is an open access article under the CC-BY-SA License.

orbital (LUMO) (Deepika et al., 2024). As the electron affinity (χ) of $FASnI_3$ is increased from 3.95 to 4.20 eV, the device performance changes are dominated by the response of Jsc and, consequently, PCE. At χ = 3.95 eV, the cell exhibits the lowest Jsc (≈27.02 mA cm^{-2}) and lowest PCE (≈28.62%), despite showing a relatively high Voc (≈1.20 V) and high FF (≈87.83%). When χ is raised to 4.00–4.10 eV, Jsc increases sharply to ≈31.65–31.67 mA cm^{-2} and the PCE reaches its maximum (~30.18%) around χ ≈ 4.05–4.10 eV, while Voc decreases to ≈1.09 V and FF decreases slightly to ~87.11–87.21%. For higher χ values (4.15–4.20 eV), both Jsc and PCE decline marginally, suggesting that the optimal band alignment window has been exceeded.Physically, varying χ shifts the perovskite conduction-band minimum (CBM) relative to the transport layers, thereby modifying the interfacial band offset and the balance between charge extraction and interfacial recombination. At low χ (3.95 eV), an unfavorable CBM alignment can introduce an electron-extraction barrier and/or increase interfacial recombination, which limits photocurrent and reduces efficiency. Increasing χ toward ~4.05–4.10 eV likely improves interfacial energetic alignment and carrier collection, explaining the strong recovery in Jsc and the corresponding rise in PCE. However, at excessively high χ, renewed energetic mismatch and transport/recombination losses can emerge, leading to the observed slight reduction in Jsc and PCE. Overall, the results indicate an optimal electron affinity range of ~4.05–4.10 eV for the simulated device stack, where the trade-off between improved charge extraction and voltage/FF losses yields the highest efficiency.

Effect of Absorber Doping, Thickness, and Bulk Defects

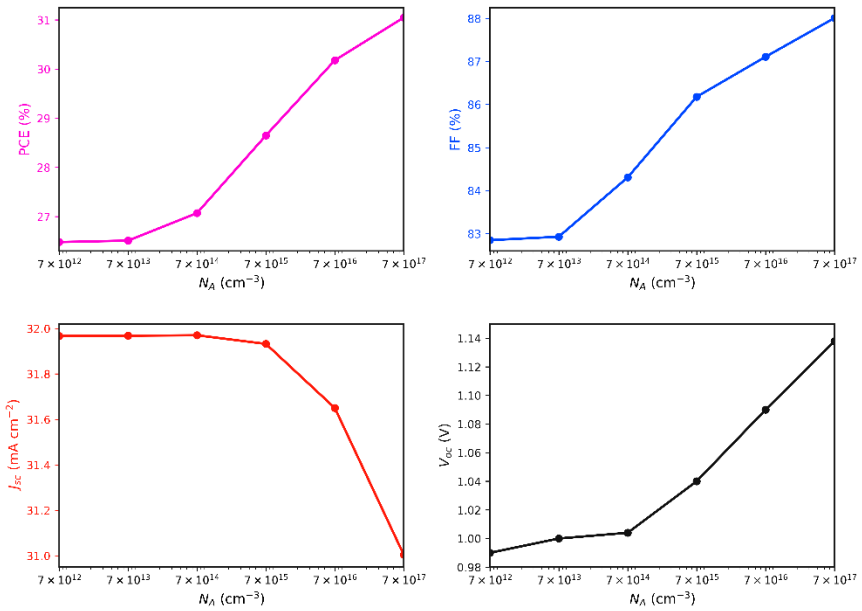

Figure 4. Impact of perovskite acceptor doping concentration (N_A) on device performance (Voc, Jsc, FF, and PCE)

Acceptor doping in the $FASnI_3$ absorber is a key lever to control the internal electric field, carrier concentration, and recombination balance, thereby influencing V_{oc}, J_{sc}, FF, and PCE. In general, increasing N_A strengthens band bending and improves hole selectivity at the HTL/absorber junction, which can enhance charge separation and suppress interfacial back-injection. However, excessively high doping may increase recombination (via higher carrier density and shorter lifetime) and can reduce the collection efficiency, particularly if transport becomes less favorable (Noman et al., 2024).

Copyright © 2026, the author(s). This is an open access article under the CC-BY-SA License.

As shown in Fig. 4, increasing N_A from 7×10^{12} cm^{-3} to $7 \times 10^{17} cm^{-3}$ results in a strong rise in V_{oc} (from 0.99 V to 1.37 V) and a monotonic improvement in FF (from 82.85% to 88.01%). This behavior indicates improved diode quality and stronger quasi-Fermi level splitting, consistent with enhanced junction selectivity and reduced recombination losses at moderate-to-high doping. In contrast, J_{sc} remains nearly constant at low-to-moderate doping and then shows a gradual reduction at higher doping (from 31.97 to 31.00 mA/cm²), suggesting that the photocurrent becomes increasingly limited by recombination/collection losses as the absorber becomes heavily doped.The combined effect produces a clear efficiency gain with increasing N_A: the PCE increases from 26.48% at 7×10^{12} cm^{-3} to a maximum of 31.05% at $7 \times 10^{17} cm^{-3}$. While the slight J_{sc} penalty at high N_A reflects emerging transport/recombination constraints, it is more than compensated by the larger improvements in V_{oc} and FF. Therefore, within the explored range, $N_A \approx 7 \times 10^{17} cm^{-3}$ provides the best trade-off for the present architecture and parameter set, and it is selected as the optimized absorber doping for subsequent simulations. At very high doping, further increases may eventually reduce PCE due to stronger recombination and reduced carrier collection; hence N_A should be optimized together with defect densities and intrinsic recombination settings.

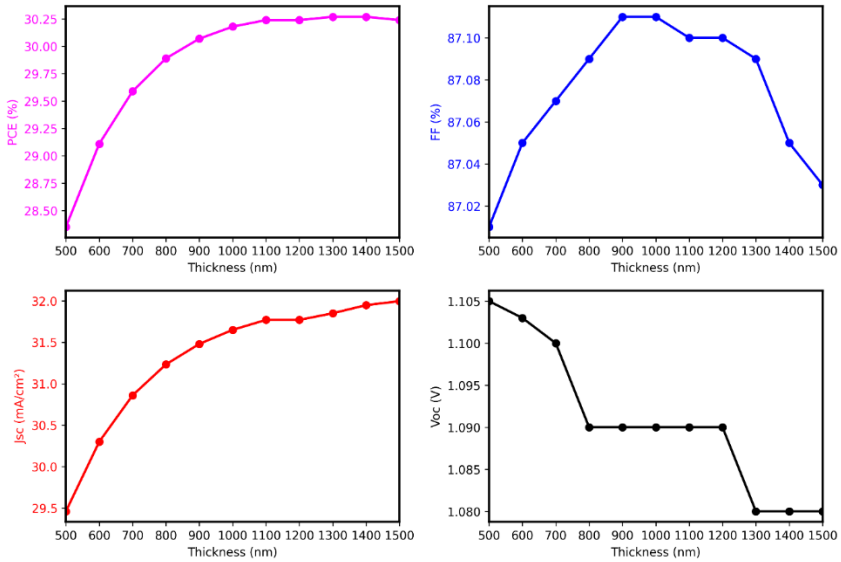

Figure 5. Impact of perovskite absorber thickness on device performance (Voc, Jsc, FF, and PCE)

Absorber thickness affects optical absorption and carrier collection in $FASnI_3$ solar cells. Increasing the thickness from 500 to 1000 nm raises J_sc from 29.46 to 31.65 mA/cm² and PCE from 28.35% to 30.18% because of enhanced light absorption. Beyond 1000 nm, J_sc gradually saturates at approximately 31.99 mA/cm², while V_oc and FF remain nearly constant at 1.08–1.105 V and 87.0–87.1%, respectively. Although the highest PCE of approximately 30.27% is obtained at 1300–1400 nm, its improvement over the 1000 nm device is marginal, indicating diminishing returns above approximately 1 µm (Hosseini et al., 2022). Therefore, 1000 nm was selected as the practical optimized thickness because it provides a favorable balance between light absorption, carrier collection, material usage, and potential recombination losses.

Copyright © 2026, the author(s). This is an open access article under the CC-BY-SA License.

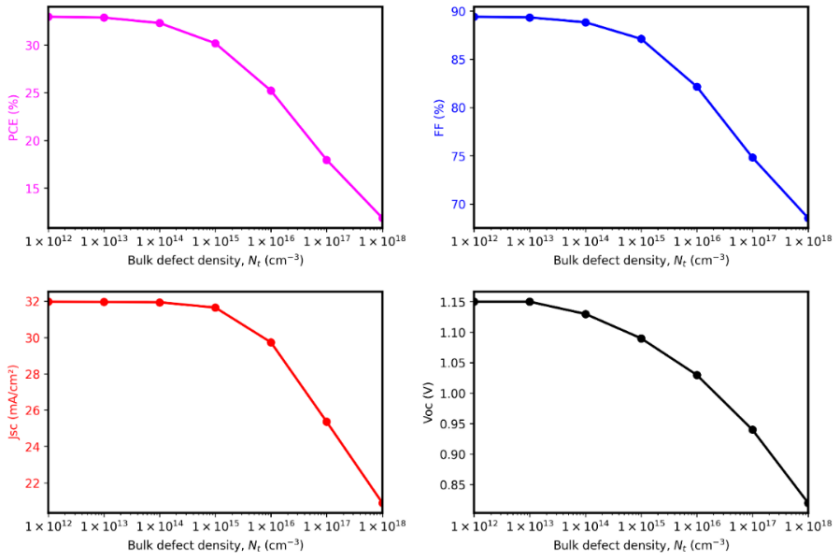

Figure 6. Effect of perovskite bulk defect density (N_t) on device performance (Voc, Jsc, FF, and PCE)

Bulk defect density in the perovskite absorber is one of the most critical parameters governing device performance because it directly controls trap-assisted Shockley–Read–Hall (SRH) recombination. Increasing $N_t$introduces more recombination centers in the absorber, reducing the effective carrier lifetime and diffusion length (Kosyachenko, 2013). As a result, photogenerated carriers are more likely to recombine before being extracted, which typically lowers V_{oc}(via reduced quasi-Fermi level splitting), degrades FF (through poorer diode quality near the maximum power point), and, at sufficiently high defect densities, also reduces J_{sc} due to incomplete carrier collection.In this study, the $FASnI_3$ bulk defect density was varied from 1×10^{12} cm^{-3} to 1×10^{18} cm^{-3}. The results reveal two distinct regimes. At low defect densities (10^{12}–10^{14} cm^{-3}), the device maintains near-ideal performance, with high V_{oc}(~1.13–1.15 V), high FF (~88.8–89.4%), and strong J_{sc}(~31.94–31.97 mA/cm²), enabling a peak PCE of 32.95% at $N_t = 1 \times 10^{12}$cm^{-3}. This indicates that SRH recombination is strongly suppressed and the device approaches an intrinsic performance ceiling. As $N_t$increases beyond 10^{15} cm^{-3}, performance degrades rapidly. At $N_t = 1 \times 10^{15}$ cm^{-3}, the PCE drops to 30.18%, accompanied by reductions in $V_{oc}$and FF. The degradation becomes severe at higher defect densities: at 10^{16}cm^{-3}, PCE decreases to 25.21% with V_{oc}falling to 1.03 V and FF to 82.17%; at 1×10^{17} cm^{-3}, the device reaches 17.96% (Voc 0.94 V, FF 74.83%); and at 1×10^{18} cm^{-3}, the PCE collapses to 11.87%, with substantial losses in both voltage and current (Voc 0.82 V, J_{sc}20.89 mA/cm²). The simultaneous drop in J_{sc}at high $N_t$confirms that carrier collection becomes strongly recombination-limited as the diffusion length becomes comparable to or smaller than the absorber thickness.Overall, the strong sensitivity of $V_{oc}$and FF to $N_t$highlights bulk SRH recombination as a dominant loss mechanism in $FASnI_3$ devices, particularly under realistic fabrication conditions. The results emphasize that reducing the bulk defect density—through improved crystallinity, compositional control, and defect passivation—is essential to approach the high-efficiency regime predicted under low-defect conditions.

Copyright © 2026, the author(s). This is an open access article under the CC-BY-SA License.

Series Resistance and Temperature Dependence

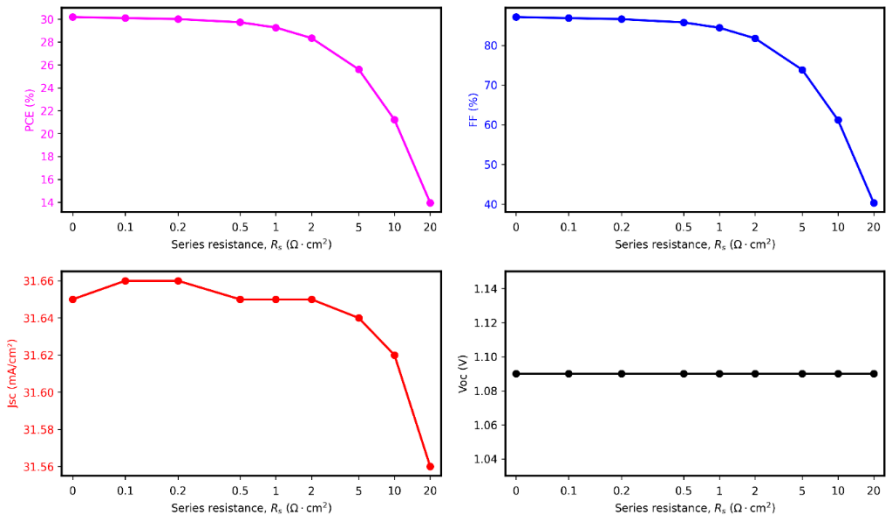

Figure 7 Effect of series resistance (R_s) on device performance (Voc, Jsc, FF, and PCE)

Series resistance (R_s) represents the lumped ohmic losses arising from the transparent contact, transport layers, interfaces, and metal contacts. In a solar cell, $R_s$primarily reduces the operating voltage under load, distorts the J–V curve near the maximum power point (MPP), and therefore degrades the fill factor (FF) and power conversion efficiency (PCE)(Fong et al., 2011). In contrast, $V_{oc}$is typically only weakly affected by $R_s$because it is measured at zero current, and $J_{sc}$is often nearly unchanged at low-to-moderate $R_s$since it is measured near zero voltage.Consistent with these expectations, increasing $R_s$from 0 to 20 Ω·cm² leaves V_{oc}essentially constant at ~1.09 V and causes only a minor reduction in J_{sc}(from 31.65 to 31.56 mA/cm²). By contrast, FF shows a strong monotonic decline from 87.11% (0 Ω·cm²) to 40.32% (20 Ω·cm²), indicating progressively stronger ohmic voltage drops and increased curvature in the J–V characteristics around the MPP. As a direct consequence, the PCE decreases substantially from 30.18% at $R_s = 0$to 29.26% at $R_s = 1$Ω·cm², and then drops more sharply at higher resistance, reaching 25.60% at $R_s = 5$Ω·cm² and 13.95% at $R_s = 20$Ω·cm².

These results demonstrate that series resistance is a dominant efficiency limiter through FF degradation, even when $V_{oc}$and J_{sc}remain nearly unchanged. Therefore, achieving high efficiency in $FASnI_3$ devices requires minimizing $R_s$via improved contact quality, higher conductivity transport layers, optimized TCO properties, and reduced interfacial resistances, particularly to preserve FF under realistic operating conditions.

Copyright © 2026, the author(s). This is an open access article under the CC-BY-SA License.

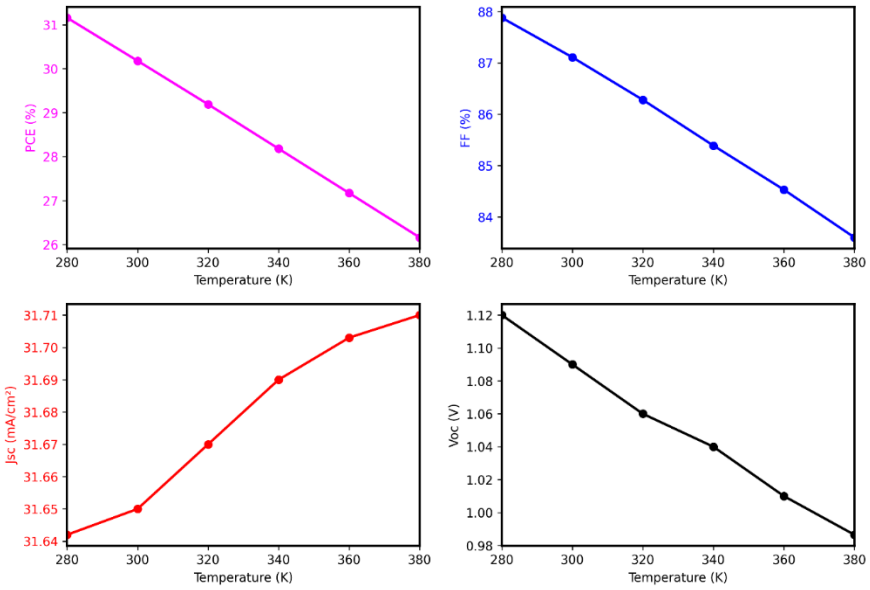

Figure 8. Temperature dependence of device performance parameters (Voc, Jsc, FF, and PCE)

Temperature is a key operational variable because it alters carrier transport and recombination kinetics, thereby shifting the diode characteristics and the maximum power point. In general, increasing temperature increases the intrinsic carrier concentration and enhances recombination, which reduces the quasi-Fermi level splitting and leads to a lower V_{oc}. Temperature can also influence FF through changes in diode ideality and resistive/transport losses, while $J_{sc}$is often comparatively less sensitive over moderate temperature ranges.Figure 8 shows the simulated device performance as the temperature increases from 280 to 380 K. A clear monotonic decline in $V_{oc}$is observed, decreasing from 1.12 V at 280 K to 0.9865 V at 380 K.

This trend is consistent with increased recombination activity at elevated temperatures and the associated reduction in quasi-Fermi level splitting. In contrast, J_{sc}remains nearly constant and increases only slightly from 31.642 to 31.71 mA/cm², indicating that photogeneration and short-circuit collection are not strongly affected within this temperature range. The fill factor decreases gradually from 87.88% (280 K) to 83.60% (380 K), reflecting a progressive deterioration of diode quality and increased thermal losses near the maximum power point.As a result of the combined reductions in $V_{oc}$and FF, the PCE decreases steadily from 31.16% at 280 K to 26.16% at 380 K. These results highlight that device performance is strongly temperature-limited primarily through voltage and fill-factor losses, emphasizing the importance of thermal management and material/interface engineering that suppresses temperature-activated recombination pathways for stable operation under practical conditions.

Copyright © 2026, the author(s). This is an open access article under the CC-BY-SA License.

DOI: https://doi.org/10.70716/reswara.v4i3.736

Interface Defects at NiO/$FASnI_3$ and $FASnI_3$/ZnO

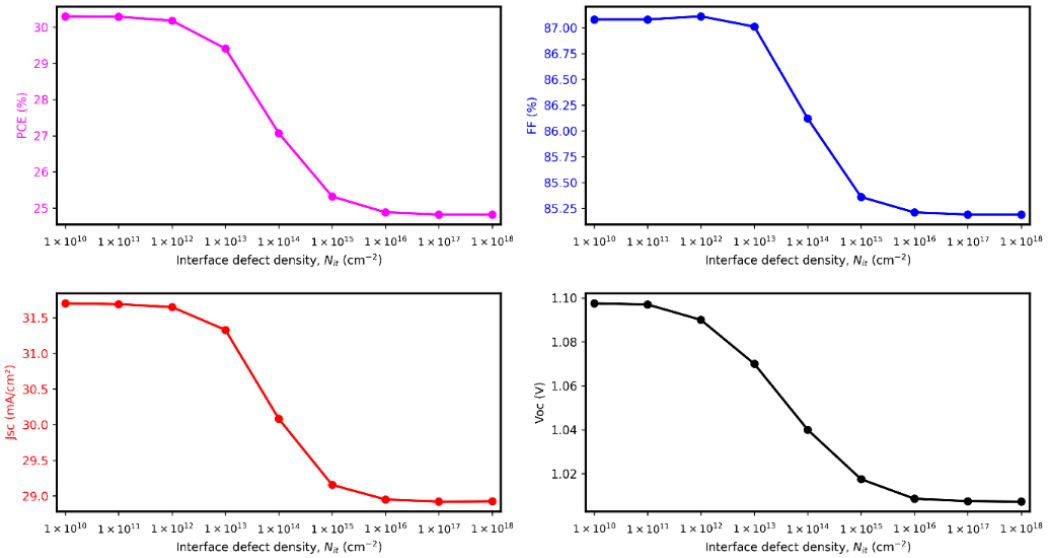

Figure 9. Effect of interface defect density (N_t) on device performance (Voc, Jsc, FF, and PCE)

Interface defects at the charge-selective contacts act as efficient recombination centers and can strongly limit device performance by enhancing trap-assisted Shockley–Read–Hall (SRH) recombination (Ateeq ul Rehman et al., 2024). In this study, the interface defect density was increased simultaneously at both dominant interfaces, NiO/$FASnI_3$ and $FASnI_3$/ZnO, to emulate coupled interfacial degradation and to isolate its impact on photovoltaic metrics. Figure 9 shows that increasing the interface defect density from to leads to a systematic performance deterioration, most prominently in and, at higher defect densities, also in . At low interface defect densities , the device maintains near-baseline performance with ≈ 1.09–1.10 V, ≈ 31.65–31.70 mA/cm², FF ≈ 87.08–87.11%, and PCE ≈ 30.18–30.30%, indicating minimal interfacial recombination losses.

Once the interface defect density reaches , begins to decline (to 1.07 V) and the PCE decreases to 29.41%, reflecting the onset of stronger interfacial SRH recombination and reduced quasi-Fermi level splitting. The degradation becomes more pronounced at , where drops to 1.04–1.0175 V, decreases to 30.08–29.16 mA/cm², and PCE falls to 27.07–25.32%. This indicates that interface recombination not only reduces and FF via poorer diode quality near the maximum power point, but also starts to impair carrier collection, lowering . For very high interface defect densities (≥), the performance approaches a saturation-like regime, with ≈ 1.007–1.009 V and PCE ≈ 24.82–24.88%, suggesting that interfacial recombination becomes strongly dominant and further increases in defect density produce diminishing incremental losses within the modeled framework. Overall, these results confirm that interface defect density is a critical performance limiter, particularly through its impact on and FF, and that effective interface passivation at both NiO/$FASnI_3$ and $FASnI_3$/ZnO is essential to sustain high efficiency under realistic fabrication conditions.

Copyright © 2026, the author(s). This is an open access article under the CC-BY-SA License.

Performance Limitation Mechanisms $FASnI_3$

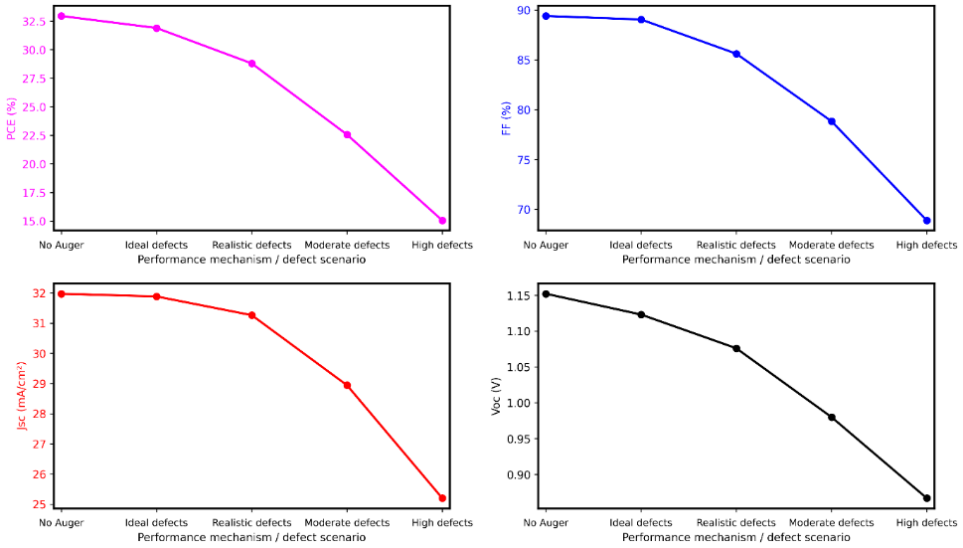

Figure 10. Performance-limitation hierarchy of the optimized $FASnI_3$ solar cell under intrinsic and realistic non-ideal conditions

The figure compares the idealized upper bound, the near-ideal low-defect case including radiative and Auger recombination, and the graded realistic scenarios (Typical, Moderate, and Pessimistic) defined by increasing bulk/interface defect densities, series resistance, and operating temperature. The progression reveals how the device transitions from an intrinsic recombination-limited regime to a practically constrained regime dominated by bulk/interface SRH recombination, with additional penalties from resistive and thermal losses.

Figure 10 consolidates the device performance evolution across progressively more restrictive operating assumptions, thereby quantifying how intrinsic recombination, defect-assisted SRH recombination (bulk/interface), resistive losses, and temperature collectively limit $FASnI_3$-based device efficiency. The upper-most benchmark is obtained when Auger recombination is not considered, yielding $V_{oc} = 1.152$,$J_{sc} = 31.97$ mA cm^{-2}, FF = 89.39%, and PCE = 32.95%. When intrinsic recombination is treated more realistically under idealized low-defect conditions (including radiative and Auger terms), the PCE decreases to 31.90% with a noticeable reduction in V_{oc}(to 1.123 V) and a small FF decrease, while J_{sc}remains essentially unchanged, confirming that intrinsic recombination primarily constrains the voltage and diode quality near the maximum power point rather than the short-circuit current.More importantly, transitioning from idealized to realistic defect scenarios produces a much larger efficiency loss, demonstrating that practical device performance is dominated by defect-assisted SRH recombination and non-ideal operational losses (Mustafa et al., 2026). In the Typical–Realistic case, the device retains a high photocurrent (31.26 mA cm^{-2}) but exhibits reduced $V_{oc} = 1.076$ V and FF = 85.61%, lowering the PCE to 28.80%. As defect densities, series resistance, and temperature are further increased in the Moderate scenario, both voltage and fill factor degrade markedly ($V_{oc} = 0.98$ V , FF = 78.83%), accompanied by a significant current loss ($J_{sc} = 28.94$ mA cm^{-2}), reducing the PCE to 22.57%. Under the Pessimistic scenario, the device becomes strongly recombination- and collection-limited, with $V_{oc} = 0.867$ V , $J_{sc} = 25.20$ mA cm^{-2} , and FF = 68.89%, yielding PCE = 15.06%. Overall, Figure 10 highlights a clear hierarchy of loss mechanisms: while intrinsic recombination slightly tightens the theoretical upper bound (mainly through $V_{oc}$and FF), the dominant efficiency gap between ideal and realistic operation is governed by bulk/interface SRH

Copyright © 2026, the author(s). This is an open access article under the CC-BY-SA License.

recombination, amplified by series resistance and temperature. This mechanistic progression provides a direct design implication: achieving experimentally realizable high-efficiency $FASnI_3$ devices requires prioritizing bulk-quality improvement (lower N_t), interface passivation (lower interface defect density), and mitigation of resistive/thermal penalties to preserve $V_{oc}$and FF under practical conditions.

Comparison with Previous Studies and Research Contribution

The trends obtained in this study are generally consistent with previous SCAPS-based investigations showing that absorber doping, defect density, interface quality, series resistance, and temperature significantly influence photovoltaic performance (Jan & Noman, 2022; Ateeq ul Rehman et al., 2024). The near-ideal PCE of 31.90% is higher than the values reported by Ateeq ul Rehman et al. (2024) and El Arfaoui et al. (2024), which were 24.87% and 19.80%, respectively. However, direct comparison should be made cautiously because each study uses different device architectures, material parameters, defect assumptions, optical models, and contact conditions. When realistic non-idealities are introduced, the PCE decreases to 28.80%, 22.57%, and 15.06% under the typical, moderate, and pessimistic scenarios, respectively. These results confirm that the near-ideal efficiency represents an upper-bound estimate rather than a directly achievable experimental value.

The novelty of this study lies in combining controlled single-parameter optimization with a graded, mechanism-resolved performance assessment under a consistent device model. This approach establishes a hierarchy of performance losses, identifying bulk and interface SRH recombination as the dominant limitations, followed by series-resistance and temperature effects. Thus, the proposed framework connects theoretical optimization with fabrication-relevant performance and provides practical priorities for absorber-quality improvement, interface passivation, contact optimization, and thermal management in $FASnI_3$ solar cells.

Limitation

This study is based on SCAPS-1D drift–diffusion simulations. Optical generation follows the built-in SCAPS formulation; therefore, absolute Jsc and PCE may shift when measured wavelength-dependent absorption, reflection, and parasitic optical losses are included. The model also uses simplified bulk and interface defect descriptions (e.g., effective trap densities and fixed defect parameters), and it does not capture perovskite-specific dynamic effects such as ion migration, hysteresis, or long-term chemical degradation of Sn-based perovskites. Consequently, the reported values should be interpreted as mechanism-resolved trends and a realistic performance window rather than a unique prediction for a specific experimental device.

CONCLUSION

This work presents a mechanism-resolved SCAPS-1D analysis of the ITO/ZnO/$FASnI_3$/NiO/Pt perovskite solar-cell architecture and clarifies how absorber energetics, defect-assisted recombination, interface quality, resistive losses, and temperature collectively determine device performance. The results show that the optimized parameter window is obtained at an absorber bandgap near 1.39 eV, an electron affinity around 4.05 eV, moderate acceptor doping, and an absorber thickness of approximately 1000 nm, together with a high-work-function back contact. Under near-ideal low-defect conditions with Shockley–Read–Hall, radiative, and Auger recombination included, the optimized device reaches $V_{oc} = 1.123$V, $J_{sc} = 31.88$ mA cm^{-2}, FF = 89.04%, and PCE = 31.90%, representing an upper-bound estimate within the adopted optical model.

Copyright © 2026, the author(s). This is an open access article under the CC-BY-SA License.

The graded realistic-defect framework further demonstrates the transition from theoretical upper-bound behavior to fabrication-relevant operation, with the efficiency decreasing from 31.90% in the near-ideal case to 28.80%, 22.57%, and 15.06% under typical, moderate, and pessimistic scenarios, respectively. These results establish a clear hierarchy of performance-limiting mechanisms in the present architecture: bulk SRH recombination and interface SRH recombination are the dominant efficiency limiters, followed by series resistance and thermal effects. Therefore, future progress in lead-free $FASnI_3$ perovskite solar cells is expected to depend primarily on improving absorber quality, suppressing interface traps, and minimizing resistive and thermal losses, rather than relying solely on increasingly idealized parameter optimization. Overall, this study provides a transferable mechanism-based framework and practical design guidance for advancing realistic high-efficiency lead-free perovskite solar cells.

ACKNOWLEDGEMENT

The author gratefully acknowledges the developers of SCAPS-1D at the Department of Electronics and Information Systems (ELIS), Ghent University, Belgium—particularly A. Niemegeers and M. Burgelman—for providing the SCAPS-1D simulation tool used in this. The author also acknowledges the support and constructive feedback from colleagues and supervisors during the preparation of this manuscript.

REFERENCES

Ahmad, K., Quasim Khan, M., Alsulmi, A., & Kim, H. (2023). Numerical Simulation and Experimental Study of Methyl Ammonium Bismuth Iodide Absorber Layer Based Lead Free Perovskite Solar Cells. *Chemistry - A European Journal*, *29*(35). https://doi.org/10.1002/chem.202300513

Aseena, S., Abraham, N., & Babu, V. S. (2020). Materials Today : Proceedings Optimization of layer thickness of ZnO based perovskite solar cells using SCAPS 1D. *Materials Today: Proceedings*, (xxxx). https://doi.org/10.1016/j.matpr.2020.09.077

Ateeq ul Rehman, A Afzal, S., Naeem, I., Bibi, D., Ghulam, S., Nabeel, F., & Obodo, R. M. (2024). Performance optimization of FASnI 3 based perovskite solar cell through SCAPS-1D simulation. *Hybrid Advances*, *7*(May), 100301. https://doi.org/10.1016/j.hybadv.2024.100301

Azhakanantham, D., Selvamani, M., Kim, T., & Kesavan, A. (2022). Exploring novel HTL suitable for Eco-friendly and high performance FASnI3 photovoltaics. *Materials Science and Engineering: B*, *284*, 115909. https://doi.org/10.1016/j.mseb.2022.115909

Chabri, I., Oubelkacem, A., Benhouria, Y., Kaiba, A., Essaoudi, I., & Ainane, A. (2023). Performance optimization of a CsGeI3-based solar device by numerical simulation. *Materials Science and Engineering: B*, *297*, 116757. https://doi.org/https://doi.org/10.1016/j.mseb.2023.116757

Deepika, Singh, A., Verma, U. K., & Ameen, S. (2024). Optimization of lead-free materials-based perovskite solar cell using SCAPS-1D simulation. *Journal of Physics and Chemistry of Solids*, *186*, 111817. https://doi.org/https://doi.org/10.1016/j.jpcs.2023.111817

El Arfaoui, Y., Khenfouch, M., & Habiballah, N. (2024). Optimization of all Pb-free perovskite CsGeI3/FASnI3 tandem solar device with 30.42% efficiency: Numerical simulation using SCAPS. *Optik*, *300*, 171638. https://doi.org/https://doi.org/10.1016/j.ijleo.2024.171638

Fong, K. C., Mcintosh, K. R., & Blakers, A. W. (2013). Accurate series resistance measurement of solar cells. *Wiley Online Library (Wileyonlinelibrary.Com)*. https://doi.org/10.1002/pip.1216

Copyright © 2026, the author(s). This is an open access article under the CC-BY-SA License.

Hosseini, S. R., Bahramgour, M., Yardani Sefidi, P., Tabatabaei Mashayekh, A., Moradi, A., Delibas, N., Hosseini, M. G., & Niaei, A. (2022). Investigating the effect of non-ideal conditions on the performance of a planar $CH_3NH_3PbI_3$-based perovskite solar cell through SCAPS-1D simulation. *Heliyon*, *8*(11). https://doi.org/10.1016/j.heliyon.2022.e11471

Hussein Sabbah, J. A. and R. M. (2022). Numerical Simulation and Optimization of Highly Stable and Efficient Lead-Free Perovskite FA 1 −. *MDPI*. https://doi.org/10.3390/ma15144761

Ibarra Michel, J., Dréon, J., Boccard, M., Bullock, J., & Macco, B. (2022). Carrier-selective contacts using metal compounds for crystalline silicon solar cells. *Progress in Photovoltaics: Research and Applications*, *31*, 380–413. https://doi.org/10.1002/pip.3552

Jan, S., & Noman, M. (2022). Influence of layer thickness, defect density, doping concentration, interface defects, work function, working temperature and reflecting coating on lead-free perovskite solar cell. *Solar Energy*, *237*, 29–43. https://doi.org/10.1016/j.solener.2022.03.069

Kosyachenko, L. A. (2013). Possibilities to decrease the absorber thickness reducing optical and recombination losses in CdS/CdTe solar cells. *Materials for Renewable and Sustainable Energy*, *2*(3), 14. https://doi.org/10.1007/s40243-013-0014-1

Lakhili, Z., & Qjidaa, H. (2024). Performance evaluation of an eco-friendly and highly efficient FASnI3-based perovskite solar cell using Mg-doped CuCrO2 as HTL. *Micro and Nanostructures*, *189*, 207816. https://doi.org/https://doi.org/10.1016/j.micrna.2024.207816

Masood Mehrabian 1, M. T.-A. 2, & 3, O. A. (2024). Using Cu 2 O/ZnO as Two-Dimensional Hole/Electron Transport Nanolayers in Unleaded FASnI 3 Perovskite Solar Cells. *MDPI*, 1–11. https://doi.org/10.3390/ma17051064

Mouchou, R. T., Jen, T. C., Laseinde, O. T., & Ukoba, K. O. (2021). Materials Today : Proceedings Numerical simulation and optimization of p-NiO / n-TiO 2 solar cell system using SCAPS. *Materials Today: Proceedings*, *38*, 835–841. https://doi.org/10.1016/j.matpr.2020.04.880

Mustafa, G., Akhtar, M., Sabir, U., Almaymoni, N., El-Fattah, W., Mnif, W., & Iqbal, M. (2026). Mechanistic insights into performance limitation and optimization of lead-free double perovskite Cs2BiAgI6 solar cells. *Journal of Sol-Gel Science and Technology*, *117*. https://doi.org/10.1007/s10971-025-07102-y

Nalianya, M. A., Awino, C., Barasa, H., Odari, V., Gaitho, F., Omogo, B., & Mageto, M. (2021). Numerical study of lead free CsSn0.5Ge0.5I3 perovskite solar cell by SCAPS-1D. *Optik*, *248*. https://doi.org/10.1016/j.ijleo.2021.168060

Njema, G. G., Kibet, J. K., & Ngari, S. M. (2025). Performance optimization of a novel perovskite solar cell with power conversion efficiency exceeding 37% based on methylammonium tin iodide. *Next Energy*, *6*(August 2024), 100182. https://doi.org/10.1016/j.nxener.2024.100182

Noman, M., Shahzaib, M., Jan, S. T., Khan, Z., Ismail, M., & Khan, A. D. (2024). Optimizing band gap, electron affinity, & carrier mobility for improved performance of formamidinium lead tri-iodide perovskite solar cells. *Materials Science and Engineering: B*, *300*, 117114. https://doi.org/10.1016/j.mseb.2023.117114

Sajid, S., Alzahmi, S., Salem, I. B., Park, J., & Obaidat, I. M. (2023). Lead-Free Perovskite Homojunction-Based HTM-Free Perovskite Solar Cells: Theoretical and Experimental Viewpoints. *Nanomaterials*, *13*(6), 983. https://doi.org/10.3390/nano13060983

Copyright © 2026, the author(s). This is an open access article under the CC-BY-SA License.

Shukla, R., Ranjan, R., & Pandey, D. S. (2021). Theoretical Study of Charge Carrier Lifetime and Recombination on the Performance of Eco-Friendly Perovskite Solar Cell. *IEEE Transactions on Electron Devices*, *PP*, 1–7. https://doi.org/10.1109/TED.2021.3078063

Singh, N. K., Agarwal, A., Singh, A. K., & Singh, S. N. (2024). Design and performance evaluation of eco-friendly FASnI3/CsSn0.5Ge0.5I3 based perovskite solar cell with distinct charge transport layer: A computational modeling. *Solar Energy*, *268*, 112256. https://doi.org/10.1016/j.solener.2023.112256

Copyright © 2026, the author(s). This is an open access article under the CC-BY-SA License.